


ITC 4/51 Information Technology and Control Vol. 51 / No. 4 / 2022 pp. 661-677 DOI 10.5755/j01.itc.51.4.30866	Fast and Robust Digital Image Spearman's Rho Correlation for Displacement Measurement	
	Received 2022/03/07	Accepted after revision 2022/08/17
	 http://dx.doi.org/10.5755/j01.itc.51.4.30866	

HOW TO CITE: Huang, W., Chen, K., Wei, W., Xiong, J., Liu, W. (2022). Fast and Robust Digital Image Spearman's Rho Correlation for Displacement Measurement. *Information Technology and Control*, 51(4), 661-677. <http://dx.doi.org/10.5755/j01.itc.51.4.30866>

Fast and Robust Digital Image Spearman's Rho Correlation for Displacement Measurement

Wanghua Huang

School of Information, Guangdong Polytechnic, Guangdong Foshan 510665, China;
Guangzhou Intelligent Building Equipment Information Integration and Control Key Laboratory,
Guangdong Guangzhou 510665, China; e-mail: gdzyhwh@qq.com

Kang Chen

Guangzhou Intelligent Building Equipment Information Integration and Control Key Laboratory,
Guangdong Guangzhou 510665, China;
School of Automation, Guangdong Polytechnic Normal University, Guangzhou Guangdong 510665, China;
e-mail: kangc0904@foxmail.com

Wei Wei

School of Computer Science and Engineering, Xi'an University of Technology, Xi'an Shanxi 710000,
e-mail: weiwei@xaut.edu.cn

Jianbin Xiong, Wenhao Liu

Guangzhou Intelligent Building Equipment Information Integration and Control Key Laboratory,
Guangdong Guangzhou 510665, China;
School of Automation, Guangdong Polytechnic Normal University, Guangzhou Guangdong 510665, China;
e-mails: xiongbianbin@gpnu.edu.cn; 563756018@qq.com

Corresponding author: kangc0904@foxmail.com

The robustness and computational efficiency of digital image correlation (DIC) are two key influencing factors for displacement field measurement applications. Especially when the speckle images are contaminated by salt-and-pepper noise, it is difficult to obtain reliable measurement results using traditional DIC methods. Digital image Spearman's Rho Correlation (DISRC), as a new DIC technique, has certain robustness to salt-and-pepper noise, but incurs a high computational load when computing subset ranks. It is found that the DISRC

can tolerate up to 15% noise level theoretically by analyzing the mean character of Spearman's Rho. Meanwhile a fast scheme is proposed in which parallelization is adopted for precomputing subset rank and computing for displacement field to accelerate the DISRC. The simulation results indicate that the fast DISRC is about 60 times faster than the original one, and the displacement field results are almost the same between them. The DISRC not only gives as well results as zero-mean normalized cross-correlation (ZNCC) without any noise, but also can tolerate 20% noise level in simulations. A case study also verifies that the result by DISRC is better than ZNCC when contaminated by smaller amounts of noise. The conclusion is that the DISRC is a strong anti-interference DIC technique, which is very important in application under complex environment, and the fast scheme is an effective way to accelerate the DISRC.

KEYWORDS: Digital image correlation; digital image Spearman's Rho correlation coefficient; salt-and-pepper noise; parallelization; Spearman's Rho.

1. Introduction

Digital image correlation (DIC) is an image processing technique used in full-field measurement methods developed from traditional speckle photography technique, and first proposed by Yamaguchi [52], Peters and Ranson [27], and Sutton et al. [39] in the 1980s. DIC is frequently used for displacement field measurements [49], structural characterizations [14-15], [40], mechanical behavior assessment [2], [5], etc. In these applications, the accuracy of DIC is frequently a research focus, including the correlation criteria. A robust digital imaging Spearman's Rho correlation (DISRC) has been proposed previously [16], but its robustness and computational optimization have been not discussed totally yet.

DIC methods can be divided into 2D-DIC (2-dimensional DIC) [28], stereo-DIC [29] and digital volume correlation (DVC) [1] in the past three decades [6], [30]. The accuracy and precision of DIC is based on three primary components: image acquisition, image analysis, and the subject of image [3]. Factors affecting the effectiveness of a DIC method include the sub-pixel intensity interpolation scheme, the subset shape function used, the image noise, the subset size and the quality of the speckle pattern [17]. During the acquisition and transmission of a digital image, various types of noise will be introduced, due to the shooting environment and image sensors. For example, thermal noise will be caused by thermal agitation of the charge carriers, fixed-pattern noise will be caused by differences between the photosensitive diodes, salt-and-pepper noise will be produced because of strong interference or failure of the analog-to-digital converter [10], etc.

Many solutions have been proposed to deal with this issue; these can be divided into two kinds: filtering of the speckle images and enlarging subset size. (1) Filtering speckle image: Pan et al. [31] proposed a 2D

Savitzky-Golay digital differentiator to calculate the strain in 2007, and then Pan [32] proposed Gaussian pre-filtering to reduce bias error in 2013. The finite element smoothing technique was investigated to enhance accuracy of displacement and strain measurement [7], [18], [25]. (2) Increasing the subset size: Pan et al. [33] adopted the sum of square of subset intensity gradients (SSSIG) to determine the size and Yaofeng and Pang [54] optimized the subset size using subset entropy. The DIC speckle pattern is the most important aspect to subset size, so various pattern assessment criteria have been proposed [11]: speckle size [55], average speckle size [19], morphological methodologies [26], [44], SSSIG [33], mean intensity gradient [34], mean subset fluctuation [20], comparison of primary and secondary peaks [45], autocorrelation peak sharpness [4], Shannon entropy, speckle distribution and size range, etc.

In addition, color can provide useful information for various computer vision tasks. In order to solve the influence of color on image characteristics caused by different lighting scenes and imaging equipment, Finlayson et al. [12] proposed a color invariant image representation method based on gray image enhancement technology to keep the order of sensor response. The key technology of eddy current pulse thermography (ECPT) is to locate and detect the surface and subsurface defects under complex geometric conditions. Chen et al. [8] proposed a three-dimensional eddy current pulse thermal imaging system, which maps thermal image to RGB-D image by matching features of thermal image and visible image. The system provides the quantitative data of 3D heat distribution, as well as the 3D spatial relationship among the defect location, the excitation coil and the whole

specimen, showing its potential for quantitative evaluation of defect characteristics.

During DIC processing, we need to calculate the correlation coefficients pixel-by-pixel, which is computationally intensive. Computational efficiency is one of the challenges in DIC techniques, and several solutions have been proposed, such as the Fast Fourier Transform (FFT) in the frequency domain to calculate zero-mean normalized cross-correlation (ZNCC) [9], [24], [30]; a reliability-guided displacement tracking scheme [35], using gradient orientation (GO) [57], sum-table approaches [21], and parallel computing [22], [36], [46], [58].

Salt-and-pepper noise is a common type of noise in digital speckle images, which often causes errors in traditional DIC techniques. DISRC was proposed as a new DIC method in our earlier studies, where the robustness to salt and pepper noise was only elementally discussed [16], [23]. In this paper, we will further discuss the robustness and the computational optimization of DISRC. Based on the statistical characteristics of Spearman's Rho (SR) [47], [50-51], DISRC can calculate the corresponding points very well even if speckle images have been contaminated by smaller amounts of salt-and-pepper noise. The DISRC can theoretically tolerate 15% level of salt-and-pepper noise. There are two main steps in SR calculation, one is calculating ranks, and the other is calculating the

correlation coefficient. Because all the SR processes in DISRC are mutually independent, the parallel computing is adopted to accelerate DISRC calculations using a Graphics Processing Unit (GPU).

The structure of the paper is as follows. The next section covers related work, including the principle of DIC, common correlation criteria, improvements for accuracy and accelerated methods. The definitions of DISRC, robustness analysis and fast scheme are presented in section 3. The robustness and acceleration are verified using artificial speckle images in section 4 and a case study is discussed in section 5. The last section concludes the paper.

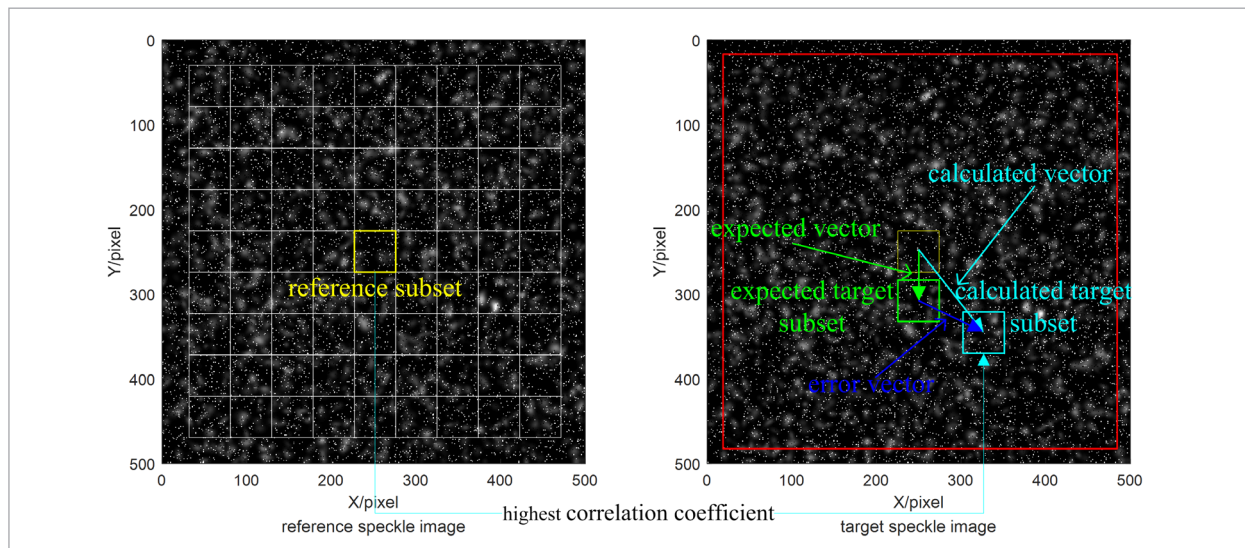
2. Related Work

2.1. Principles of DIC

A reference speckle image and a target speckle image are acquired before and after object deformation. A $(2M+1) \times (2M+1)$ subset is obtained from the reference speckle image. Then, a search operation is performed on the region of interest in the target speckle image to determine the target subset that correlates best with the reference subset. The center of the target subset is considered to map to the center of the reference subset. A standard subset DIC is illustrated in Figure 1. Firstly, the reference speckle image is separated into many

Figure 1

Subset DIC frame



non-overlapping and continuous subsets, and the center of each subset is denoted as a reference point. For example, if the subset size is 51×51 pixels, 81 subsets will be captured from a 500×500 pixel reference speckle image. Then, a pixel-by-pixel search on the region of interest of the target speckle image is performed to determine the target subset that yields the highest correlation coefficient compared to the reference subset. Lastly, the sub-pixel is calculated by the gradient algorithm [37]. The center of the target subset is the target point. The vector from the reference point to the target point is called a calculated vector. Finally, to quantitatively analyze the performance of the simulation results, the mean and variance of the error vector magnitude (EVM) [48] between the calculated vector and the assumed vector will be calculated.

2.2. Correlation Criteria

Many correlation criteria have been proposed to evaluate the similarity between the reference subset and the target subset. Pan et al. [38] classified these criteria into four categories: cross correlation, sum of absolute differences, sum of squared differences, and parametric sum of squared differences. Except from the sum of absolute differences, which is less practical and thus rarely used, the other three types have many varieties, as shown in Table 1 [30]. The abbreviation Z stands for zero-mean processing, and the abbreviation N stands for normalized processing. $\bar{r} = \frac{1}{n} \sum_{i=1}^n r_i$, $\bar{t} = \frac{1}{n} \sum_{i=1}^n t_i$, $n = 2M + 1$, $\bar{r}_i = r_i - \bar{r}$, $\bar{t}_i = t_i - \bar{t}$, two unknown parameters a and b .

Table 1

Three types of correlation criteria

Cross correlation (CC)	Squared differences (SSD)	Parametric sum of squared differences (PSSD)
$C_{CC} = \sum r_i t_i$	$C_{SSD} = \sum (r_i - t_i)^2$	
$C_{ZCC} = \sum \bar{r}_i \bar{t}_i$	$C_{ZSSD} = \sum (\bar{r}_i - \bar{t}_i)^2$	$C_{PSSD_b} = \sum (r_i + b - t_i)^2$
$C_{NCC} = \frac{\sum r_i t_i}{\sqrt{\sum r_i^2} \sqrt{\sum t_i^2}}$	$C_{NSSD} = \sum \left(\frac{r_i}{\sqrt{\sum r_i^2}} - \frac{t_i}{\sqrt{\sum t_i^2}} \right)^2$	$C_{PSSD_a} = \sum (a r_i - t_i)^2$
$C_{ZNCC} = \frac{\sum \bar{r}_i \bar{t}_i}{\sqrt{\sum \bar{r}_i^2} \sqrt{\sum \bar{t}_i^2}}$	$C_{ZNSSD} = \sum \left(\frac{\bar{r}_i}{\sqrt{\sum \bar{r}_i^2}} - \frac{\bar{t}_i}{\sqrt{\sum \bar{t}_i^2}} \right)^2$ $= 2(1 - C_{ZNCC})$	$C_{PSSD_{ab}} = \sum (a r_i + b - t_i)^2$ $= \sum \bar{t}_i^2 (1 - C_{ZNCC}^2)$

2.3. Accuracy Improvements

In order to obtain accurate displacement and strain measurements, Pan et al. [31] used the two-dimensional Savitzky-Golay digital differentiator to fit the displacement components, which were calculated using Newton-Raphson. This allows the avoidance of greater strain error because of tiny displacement bias error caused by noise. Gaussian pre-filtering has also been used to reduce the level of speckle image noise, so the interpolation error due to image noise is decreased accordingly [32]. Finite element smoothing technique was developed for both displacement and strain analysis by Segalman et al. [42] and Sutton et al. [43]. Sun et al. [41] proposed a finite element formulation for digital image correlation, while Zhao et al. [56] investigated a finite element method and Tikhonov regularization for smoothing noisy displacement fields. Yang [53] developed finite element digital image correlation for irregular displacement fields.

The effect of subset size on the accuracy of DIC has been thoroughly investigated by many researchers. Yaofeng and Pang [54] proposed a parameter called subset entropy, which is the average of absolute intensity deviations at any point in the subset from its neighboring 8 points, which then normalized. Based on the relation between subset entropy and displacement errors, a larger subset size was advised for underlying actual deformations. Pan et al. [33] proposed the SSSIG, and gave a threshold of 1×10^{-5} to select suitable subset size.

The speckle pattern is an important factor that affects the accuracy of DIC, which can be traced back to the image noise. Image noise and other specimen surface conditions determine the speckle pattern quality. The assessment criteria of speckle pattern are divided into local and global to assess subset and global speckle respectively [11]. Hua et al. [20] evaluated the quality of speckle pattern by mean subset fluctuation, and found that speckle size and density have an influence on the quality of speckle pattern. Bomarito et al. [3] proposed a digital image correlation pattern optimization based on SSSIG and the secondary auto-correlation peak height. Lecompte et al. [26] proposed a speckle size distribution based on image morphology, and subsequently the relationship between the mean speckle size and the subset size was verified.

2.4. Acceleration Methods

Computational efficiency is an important issue to DIC, and many fast solutions have been proposed. Chen et al. [9] initially introduced a two-step FFT for displacement measurement, and Jiang et al. [24] adapted the FFT to calculate cross-correlation for integer-pixel registration. Pan [35] proposed a reliability-guided displacement tracking strategy using improved an initial guess transfer scheme, to avoid redundant computations. Zhong and Quan [57] used the GO technique to determine the potential target point. A pre-calculated sum-table scheme has been utilized for normal cross correlation (NCC), which allows the calculations of image mean, image variance and cross-correlation between images to be invariant to the size of subset window [21].

There are two kinds of parallel computing methods: those utilizing the GPU or multi-threaded methods. Zhang et al. [58] implemented a path-independent DIC method using the GPU, including integer-pixel and sub-pixel displacement values' processing. Huang et al. [22] proposed programming models for GPU and CPU parallel computing, in which the CPU also perform tasks, such as calculating the integer-pixel and sub-pixel displacement. Pan and Tian [36] improved the reliability-guided digital image correlation using multi-threading, and Shao et al. [46] proposed a seed point-based parallel method to calculate the sub-pixel using multi-threading.

3. Robustness Analyses and Fast DISRC

3.1. DISRC

Let $\{(r_i, t_i)\}_{i=1}^n$ denote the pair of reference speckle subset image R and target speckle subset image T , r_i and t_i are the gray values, n is the number of image pixel, $n = 2M + 1$. We regard the two images as a bivariate Gaussian model, i.e. the pixel pairs are independent and identically distributed data pairs drawn from a bivariate population with a continuous joint distribution. Let p_i be the rank of r_i and q_i be the rank of t_i , while P and Q are the sets. The DISRC between R and T , denoted by $C_{sr}(R, T)$, is defined as follows [51]:

$$C_{sr}(R, T) \triangleq 1 - \frac{6 \sum_{i=1}^n (p_i - q_i)^2}{n(n^2 - 1)}. \quad (1)$$

The C_{sr} has the following general properties:

- 1 Standardization: $-1 \leq C_{sr} \leq 1$.
- 2 Symmetry: $C_{sr}(R, T) = C_{sr}(T, R)$.
- 3 $C_{sr} = \pm 1$, if R is a positive (negative) linear transformation of T .
- 4 $C_{sr} = 0$, if R and T are independent.
- 5 $C_{sr}(R, T)$ converges to a normal distribution when the image size n is large enough.

The parent of $\{(R, T)\}$ (*i.i.d.*) is also a bivariate Gaussian distribution, whose density function is:

$$\phi(R, T) = \frac{1}{2\pi\sigma_R\sigma_T} \exp\left[-\frac{z}{2(1-\rho^2)}\right], \quad (2)$$

where $z = \frac{(R - \mu_R)}{\sigma_R} - \frac{2\rho(R - \mu_R)(T - \mu_T)}{\sigma_R\sigma_T} + \frac{(T - \mu_T)}{\sigma_T}$, ρ is the correlation coefficient between R and T , μ_R and μ_T are the gray means of the reference image R and target image T , respectively, while σ_R^2 and σ_T^2 are the corresponding gray variances.

The above bivariate Gaussian model can be expressed as follows:

$$(R, T) \sim N(\mu_R, \mu_T, \sigma_R^2, \sigma_T^2, \rho). \quad (3)$$

When the two speckle images are contaminated by a tiny fraction of salt-and-pepper noises (with huge

variance) as described in section 1, the following contaminated Gaussian model represents the probability density function of the two contaminated speckle images [47].

$$CN(\rho, \rho') \triangleq (1-\varepsilon)N(\mu_R, \mu_T, \sigma_R^2, \sigma_T^2, \rho) + \varepsilon N(\mu'_R, \mu'_T, \sigma'^2_R, \sigma'^2_T, \rho') \quad (4)$$

where $0 < \varepsilon < 0.5$, $-1 \leq \rho \leq 1$, $-1 \leq \rho' \leq 1$, ρ is the population correlation coefficient between the two "clear" speckle images, and ρ' is the population correlation coefficient between the parts of salt-and-pepper noise in the two speckle images. $CN(\rho, \rho')$ is strongly biased with regard to ρ , i.e. for any $\varepsilon > 0$, there exists

$$\lambda = \frac{\sigma'^2_R}{\sigma_R^2} = \frac{\sigma'^2_T}{\sigma_T^2} \gg 1.$$

3.2. Robustness Analysis

Studies on the correlation of bivariate contaminated Gaussian model by Xu et al. [51] proved that when ε is sufficiently small, the approximate mean of the SR correlation coefficient in a bivariate Gaussian model is as follows:

$$\lim_{\substack{n \rightarrow \infty \\ \lambda_R \rightarrow \infty \\ \lambda_T \rightarrow \infty}} E(C_{sr}) \approx \frac{6}{\pi} \left[(1-3\varepsilon) \arcsin \frac{\rho}{2} + \varepsilon \arcsin \rho' \right]. \quad (5)$$

The mean of C_{sr} between the reference and target speckle images is composed of ρ and ρ' , and as $n \rightarrow \infty$, $\lambda \rightarrow \infty$. To guarantee that the correlation result is decided mainly by ρ , the set of inequalities are obtained from Equation (5).

$$\begin{cases} (1-3\varepsilon) \arcsin \frac{\rho}{2} > 0 \\ (1-3\varepsilon) \arcsin \frac{\rho}{2} > \varepsilon \arcsin \rho'^2 \end{cases} \quad (6)$$

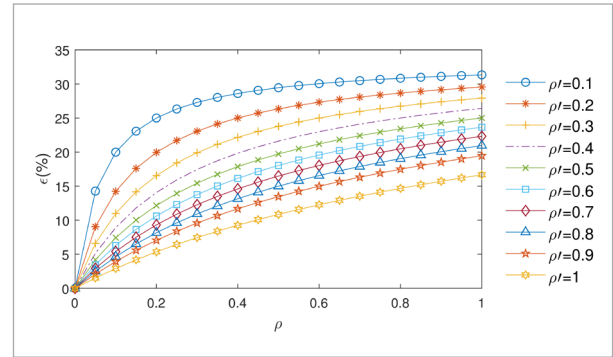
Here we only consider the situation where $\rho > 0$ and $\rho' > 0$. ε will increase as ρ and ρ' increase as shown in Figure 2. For example, when $\rho' = 1$ and $\rho > 0.85$, the DISRC can tolerate 15.2% level of salt-and-pepper noise theoretically.

3.3. Fast DISRC Scheme

The computational efficiency of DIC is a bottleneck for real time processing, and the DISRC suffers from

Figure 2

The percentage that DISRC can tolerate under different correlation coefficients



the same problem. We improve the DISRC computational efficiency in two aspects: subset rank pre-computation and parallelization. After loading the reference and target speckle images, all the subset ranks are precalculated in parallel first. And then the displacement field calculations including correlation coefficient calculation and sub-pixel calculation, are also parallelized.

1 Precomputing Subset ranks by parallelization

Precomputation is a common fast solution in digital image correlation methods [22]. The target subset ranks will be required over and over again when searching in the ROI for target subset most similar to each reference subset. For example, if there are L reference subsets, the same target subset ranks will be calculated L times. Precalculated ranks thus reduce the calculation times. All ranks of reference subsets and target subsets are computed primarily by sorting the gray level values, and the subset rank operation has $O(n \log_2 n)$ time complexity. All of precalculated ranks of the reference and target subsets could be computed in parallel using vectorization, multi-threading or through the GPU, because of independent from each other. Figure 3 is the parallel calculation frame of subset ranks. Subsets are extracted from the reference and target images, and then subset ranks are calculated using parallel computing.

2 Parallelization of displacement field computation

The purpose of the DIC technique is to determine the displaced position of every point in reference speckle image, and all of these processes are independent of each other. As known from Equation 1, the correlation

Figure 3
Precomputing subset ranks by parallelization

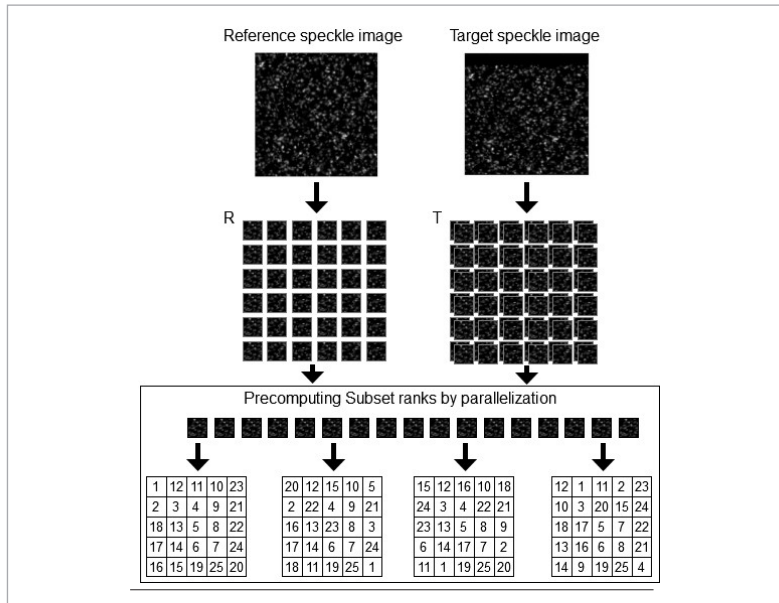
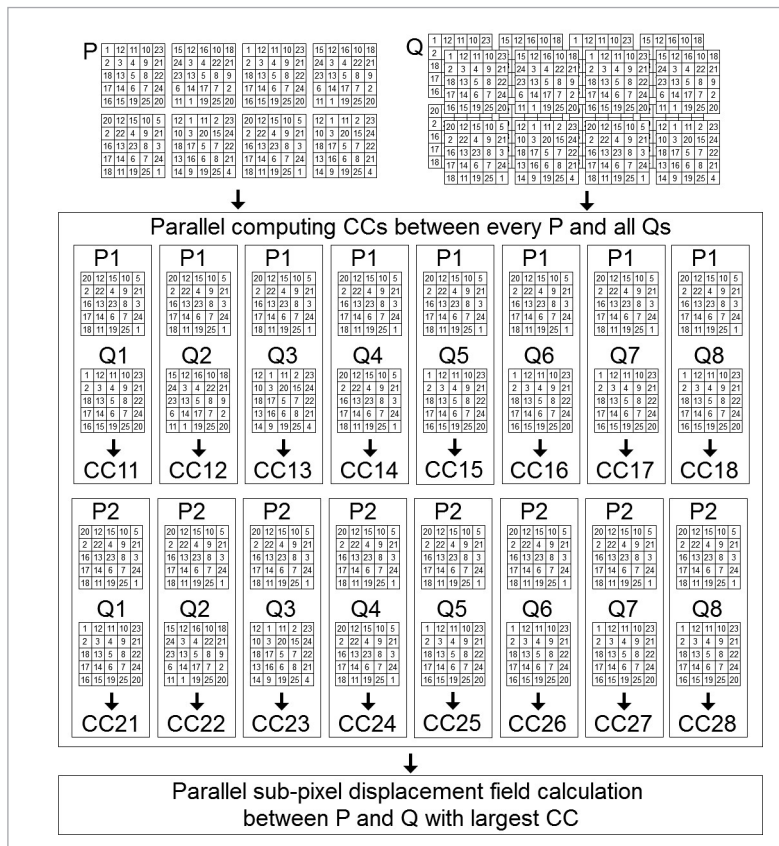


Figure 4
Parallel calculation of displacement field



coefficient calculation of SR includes subtraction and accumulation between P and Q ranks, which has only $O(n)$ time complexity. The above calculations are mutually independence, and can thus be parallelized as shown in Figure 4. Firstly, the integer-pixel displacement is determined by the position of the maximum correlation coefficient between the reference subset and the target subset. These subsets are located in the region of interest of the target speckle image. And then the sub-pixel displacement field calculation is parallelized again for high precision.

Therefore our fast DISRC parallel computation includes two parts: the pre-ranks of the reference and target subsets are calculated; and then high-precision displacement field is computed between a same reference subset and every target subset in region of interest of target speckle image.

Of course, the computational efficiency of parallelism is related to the CPU cores and RAM space of the hardware device. The more CPU cores and higher CPU frequency, there will be higher the computational efficiency of parallelism. According to Amdahl's law [13], the maximum speedup that can be achieved using N number of processors is $S = 1 / [(1 - \rho) + (p / N)]$, where p is the parallelism rate. At the same time it need more RAM space and time for storing data, for example, n (the number pixels of subset) times of space will be occupied at least for target subset ranks.

4. Simulation

To verify the robustness of the DISRC and to implement parallel processing, we performed displacement

measurement simulation, and implemented a displacement field case, both on a server, with two 12-core CPUs and 32G RAM, Window server 2012 and Matlab 2018. In the following simulations, speckle images will be generated with small or no amounts of salt-and-pepper noise. All DISRC simulation results will be compared with only ZNCC, because the ZNCC has the linear relationship between ZNSSD and PSSD. As shown in Table 1, according to the equation $C_{ZNSSD} = 2(1 - C_{ZNCC})$, we can easily find that there is a linear relationship between ZNSSD and ZNCC. However, for the PSSD, although the linear relationship between the PSSD and the ZNCC is not explicitly shown in the equation $C_{PSSD,ab} = \sum \bar{I}_i^2 (1 - C_{ZNCC}^2)$, if we take $\sum \bar{I}_i^2$ as constants, mathematical inferences show that they have a simple linear relationship with the partial derivatives of the desired deformation parameter vector [30].

4.1. Speckle Image Generation

In order to verify the robustness of DISRC and its tolerance- to salt-and-pepper noise, the “clear” reference and target speckle images were artificially contaminated by a certain amount of salt-and-pepper noise, and then the target speckle image was linearly compressed. All “clear” speckle images were generated using the expression proposed in [59], as shown in following. Furthermore, the size and self-rotation angle of each speckle granule were randomized values in order to increase the difference between subsets. The mathematical models of the “clear” speckle images are as follows:

Reference speckle image:

$$F(x, y) = \sum_{i=1}^M L_i \exp\left(-\frac{\mu^2}{O_x^2} - \frac{v^2}{O_y^2}\right). \quad (7)$$

Target speckle image:

$$G(x, y) = \sum_{i=1}^M L_i \exp\left(-\frac{\mu'^2}{O_x^2} - \frac{v'^2}{O_y^2}\right), \quad (8)$$

$$\text{where } \begin{bmatrix} \mu \\ v \end{bmatrix} = \begin{bmatrix} \cos \theta & \sin \theta \\ -\sin \theta & \cos \theta \end{bmatrix} \begin{bmatrix} x - x_i \\ y - y_i \end{bmatrix}; \quad \begin{bmatrix} \mu' \\ v' \end{bmatrix} = \begin{bmatrix} \cos \theta & \sin \theta \\ -\sin \theta & \cos \theta \end{bmatrix} \begin{bmatrix} x - x_i - \mu_i \\ y - y_i - v_i \end{bmatrix};$$

M is the total number of speckle granules; L_i is a random value indicating the peak intensity of the i th

speckle granule; O_x and O_y are the width of the asymmetrical radial basis function (ARBF) on the x and y axes, respectively; θ is the self-rotation angle; (x_i, y_i) represents the center location of the i th speckle granule before deformation; and p_x and p_y are the compression rates of the target speckle image along the x and y directions, respectively.

The parameters of the speckle images used for this study are as follows: (1) the size of the speckle images was 500×500 ; (2) the number of speckle granules was $M = 1800$; (3) the ARBF width, $O_x \in [3, 6]$ and $O_y \in [3, 6]$; (3) the self-rotation angle was in the range $\theta \in [-45^\circ, 45^\circ]$; (4) the compression rates were $p_y = 95\%$ and $p_x = 0$. The reference and target speckle images are contaminated using salt-and-pepper noise of the same density. For example, Figure 1 shows the reference and target speckle images with a salt-and-pepper noise level of 6%.

In the following simulations, non-overlapping and continuous reference subsets are captured from the reference speckle image, and the center of each subset is denoted as the reference point. For example, 81 subsets are captured from a 500×500 reference speckle image when the subset size is 51×51 , and this is a suitable size as determined by SSSIG. The whole target speckle image is regarded as the ROI. and a pixel-by-pixel search operation for the target sub-block is performed on the target speckle image based on the criterion of correlation coefficient, followed by a sub-pixel calculation using the gradient algorithm [38]. The center of the target subset is also denoted as the target point. Finally, both of the average and the variance of the EVM are computed.

4.2. Fast DISRC Results and Analysis

The fast DISRC algorithm was directly paralleled by the cellfunc function in Matlab, including precomputing subset ranks and sub-pixel displacement field. The ZNCC was parallelized in the same way: the zero-mean normalization of gray values was precomputed parallelly, and then correlation coefficients and sub-pixel displacement field were also computed in parallelism. The displacement field result errors between fast and original DISRC or ZNCC were about 1×10^{-5} , so our fast scheme will not affect the precision. As shown in Table 2, the runtime comparison of two main methods in DISRC and ZNCC respectively, we can find that computing rank took 42 times longer

Table 2

Runtime of main methods in DISRC and ZNCC, subsize: 51×51. unit: second

Computing rank in DISRC	Correlation coefficient in DISRC	Zero-mean normalization in ZNCC	Correlation coefficient in ZNCC
6.0942×10^{-4}	1.4359×10^{-5}	2.9292×10^{-5}	2.1198×10^{-5}

than correlation coefficient in DISRC, while it just spent almost the same time between computing zero-mean normalization and correlation coefficient in ZNCC. So it is quite essential to compute subset ranks in advance, otherwise it will spend a lot of time, which hamper popularization and application of SR.

Figure 5 shows the mean runtime of different subsets size between fast or not DISRC and ZNCC, which were done in our hardware and software environment. All of the runtime included subset rank pre-computation, correlation coefficient computation and gradient algorithm sub-pixel displacement, all of which were run in parallelism. Figure 5 (a) shows the comparison between fast and original DISRC, where the left axis is for fast DISRC and the other is for original DISRC. Fast DISRC was about 60 times faster than the original one averagely, but it would become smaller as the subset size increase. Because the number L of reference subset will be smaller as the size increase, the times L need to recomputed the same target subset rank will be smaller in original DISRC. Figure 5 (b) shows the runtime comparison between fast and original ZNCC, but the fast ZNCC was only about 2 times faster than the original one, which effect was not as well as fast DISRC. The fast DISRC spent less time than fast ZNCC, known as in Figure 5 (a) and (b), because ZNCC requires three times as many multiplications operations as DISRC does. And it help DISRC in popularization and application.

4.3. Simulation Result and Analysis

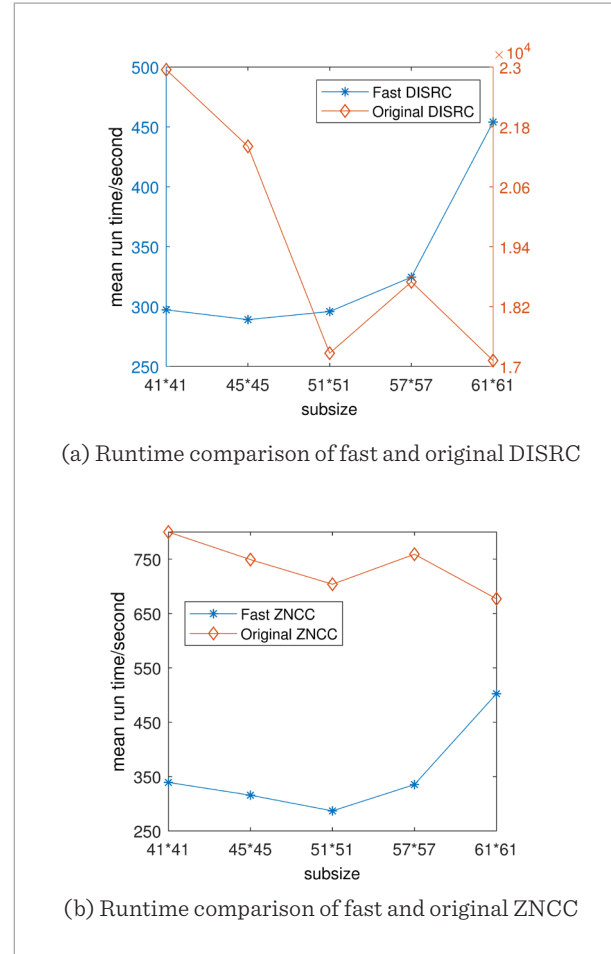
1 Comparisons between DISRC and ZNCC

(1) Monolithic translation

To verify the feasibility and robustness of DISRC, two comparisons between DISRC and ZNCC were performed: speckle images without noise and images contaminated by 10% of salt-and-pepper noise; the target speckle image was displaced 5.345 pixels from the reference speckle image only along y -di-

Figure 5

Runtime comparison of fast and original algorithms



rection. The subset size is only 51×51 in this section. The results are shown in Figure 6 and table 3. Figure 6 (a) and (b) are the noiseless versions, while the others are the contaminated versions. Table 3 shows the corresponding values of the mean and variance of the EVM.

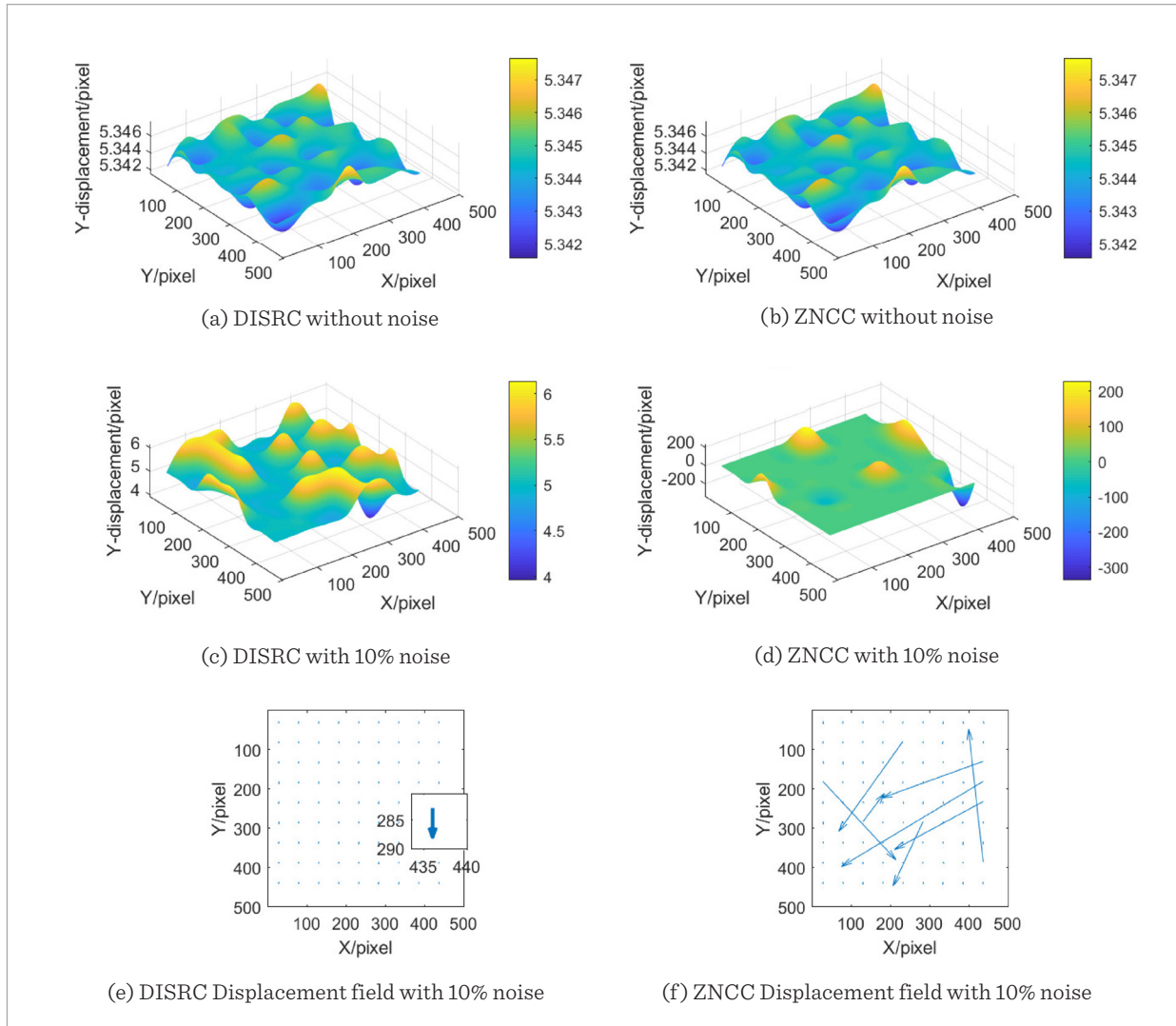
Table 3

Mean and variance of EVM with monolithic translation

	Noiseless		Contaminated by 10% salt-and-pepper noise	
	DISRC	ZNCC	DISRC	ZNCC
Mean	0.0014	0.0014	0.5222	27.1285
Variance	7.5178×10^{-7}	7.5178×10^{-7}	0.0749	7.0175×10^3

Figure 6

Comparison between DISRC and ZNCC with monolithic translation



ZNCC is one of classical DIC criteria, the result of which is accepted by most of scholars. As shown in Figure 6 (a) and (b), the y directional displacements both using DISRC and ZNCC are about 5.344 pixels, which are approximately to the expected value 5.345 pixels. The mean and variance of the EVM are very small, in this case, as shown in Table 3, where the mean is only 0.0014 and the variance is 7.5178×10^{-7} the both cases.

Figure 6 (c)-(f) and Table 3 are the results obtained when the speckle images are contaminated by 10%

salt-and-pepper noise, which mainly affects ZNCC. Figure 6 (c) and (d) are the y -directional displacements both using DISRC and ZNCC. DISRC is more robust than ZNCC, because the corresponding means and variances of the EVM are smaller robust than ZNCC. It is also very clear in Figure 6 (e) and (f) where the displacement vectors of DISRC are very consistent while some vectors using ZNCC are chaotic.

(2) Linear compression

Another two comparisons between DISRC and ZNCC were performed for linear compression when speck-

le images are without noise or contaminated by 10% salt-and-pepper noise. The subset size was again 51×51 , and the results are shown in Figure 7 and Table 4. The y -direction displacements by DISRC and ZNCC without noise are shown in Figure 7 (a) and (b), which close to expected value. The mean and variance of EVM are small as shown in Table 4.

When the speckle images are contaminated by 10% salt-and-pepper noise, the result by DISRC is still very good as shown in Figure 7 (c) and (e), and the mean and variance of EVM are only 0.4894 and 0.1438 respectively. However, for ZNCC as shown in Figure 7 (d) and (f), many vectors point to wrong positions,

and the means and variances of EVM are 64.8649 and 1.7903×10^4 , as shown in Table 4.

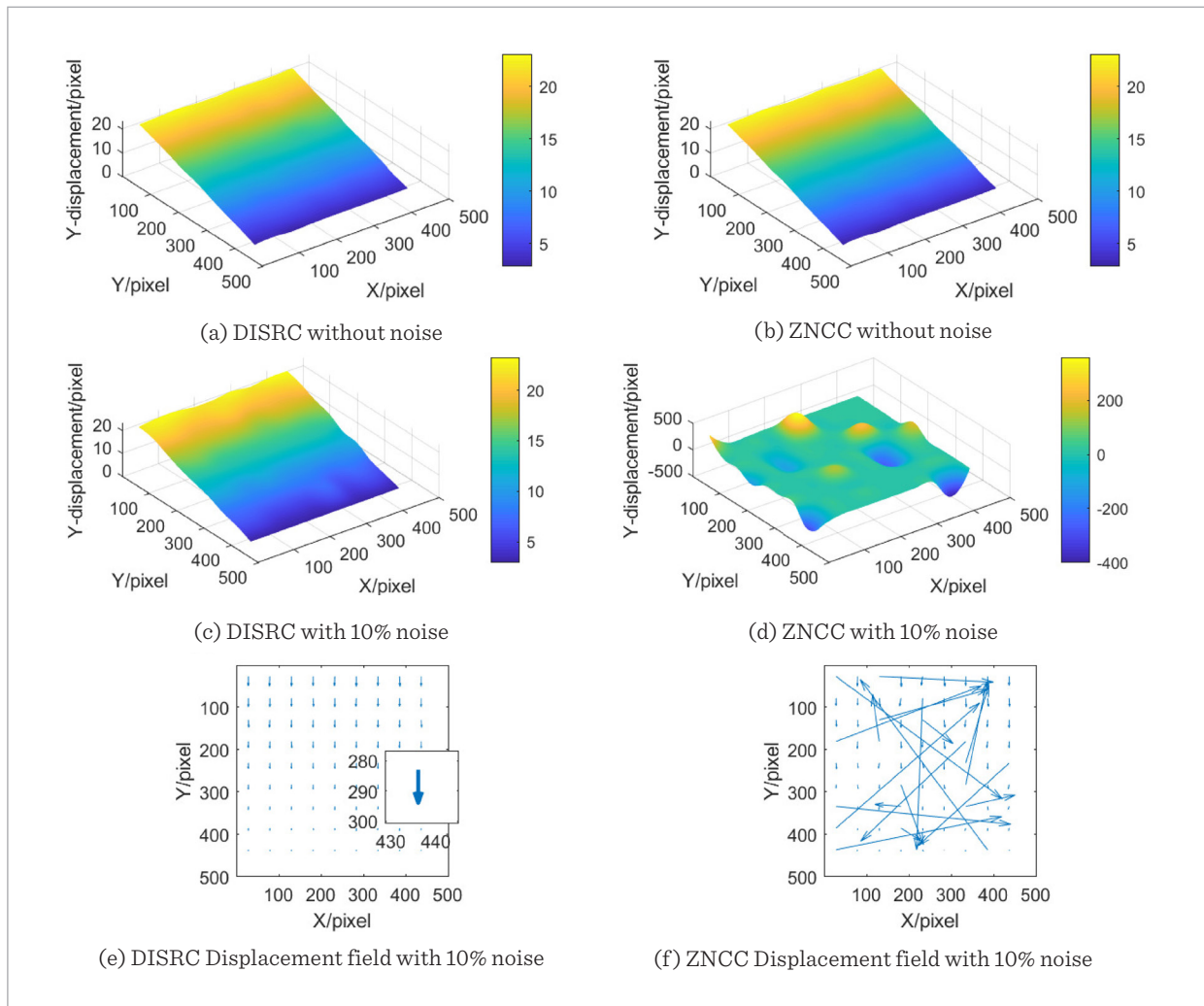
Table 4

Mean and variance of EVM with linear compression

	Noiseless		Contaminated by 10% salt-and-pepper noise	
	DISRC	ZNCC	DISRC	ZNCC
Mean	0.1889	0.1962	0.4894	64.8649
Variance	0.0110	0.0129	0.1438	1.7903×10^4

Figure 7

Comparison between DISRC and ZNCC with linear compression



Two conclusions can be drawn from the above two sections: (1) DISRC shows the same results as ZNCC in the absence of noise. (2) DISRC is more robust to salt-and-pepper noise than ZNCC, as the displacement field of DISRC is almost the same as the expected ideal one.

2) Comparisons between different noise levels

To verify the robustness of DISRC, Figure 8 shows the comparison results for different levels of salt-and-pepper noise. The subset size was 51×51 , and the noise levels varied from 1%-21% at 2% increments. The ZNCC was robust to a certain extent when noise levels were 1% and 3%, but results were poor when the level was larger than 5%, as shown in Figure 8 (a). However, the DISRC can tolerate to 21% noise level as shown in Figure 8 (b), in which all of the vectors pointed to correct positions. As shown in Figure 9, when the noise is amplified to 30%-40%, the direction of the vector in the figure deviates and cannot point to the correct position, thus losing its application value.

The DISRC may provide satisfactory results for even higher density noise, but this, in our opinion, is not significant. The correlation coefficient reduces as the noise level increases, as shown Figure 8 (c), but if it is less than 0.5, sufficient accuracy for engineering applications cannot be ensured. At 3% noise level, it is already 0.4404 for ZNCC, while it is still 0.5419 when the noise level is 15% for DISRC.

The EVM is an important factor to evaluate the calculation result, and the mean of EVMs for DISRC and ZNCC at different noise density levels are shown in Figure 8 (d) (left axis for DISRC and right axis for ZNCC). The mean is less than 1 for DISRC even when the noise level is up to 21%, while it is about 135 for ZNCC. The calculation result using DISRC is more stable than ZNCC, as the EVM variance using DISRC is less than 0.25 even with 21% noise, shown in Figure 8 (e). And it is up to 2750 using ZNCC with only 5% noise as shown in Figure 8 (f).

Figure 8

Comparison between different noise levels, subset size: 51×51

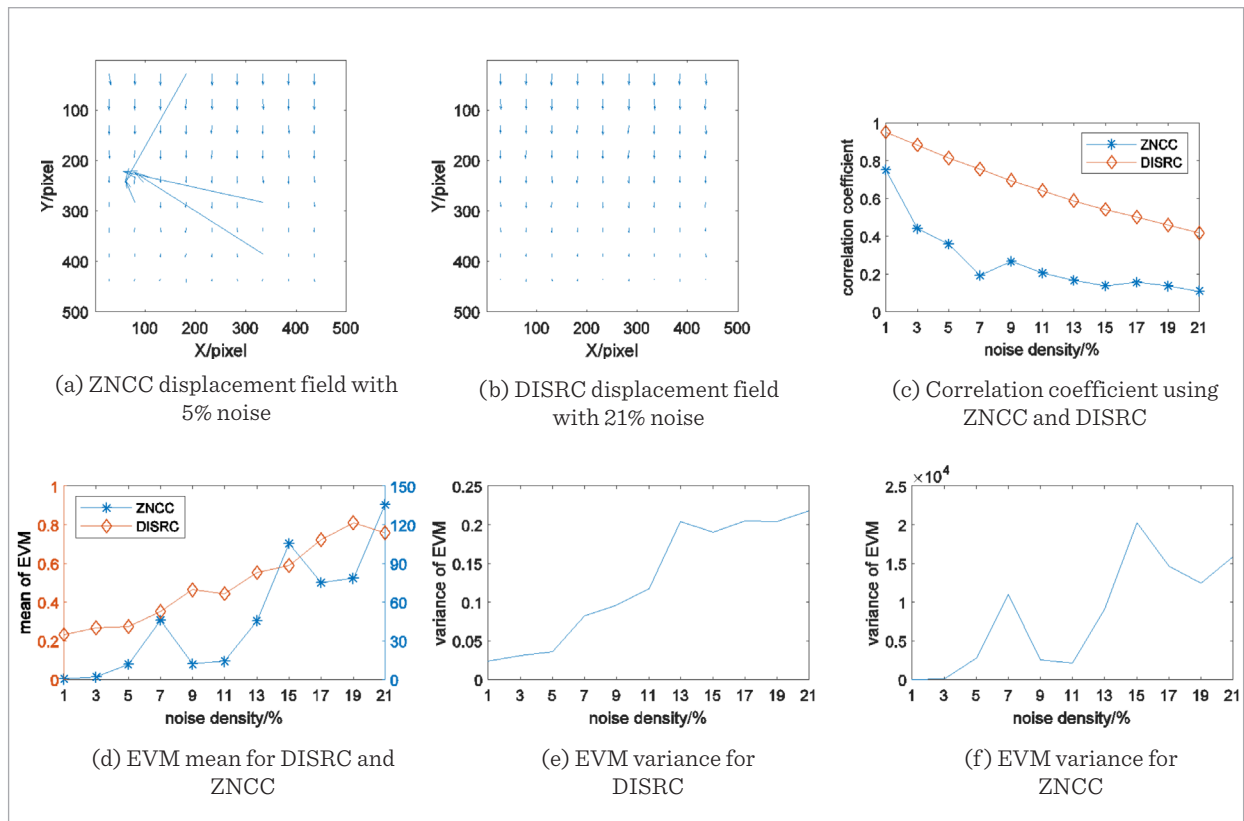
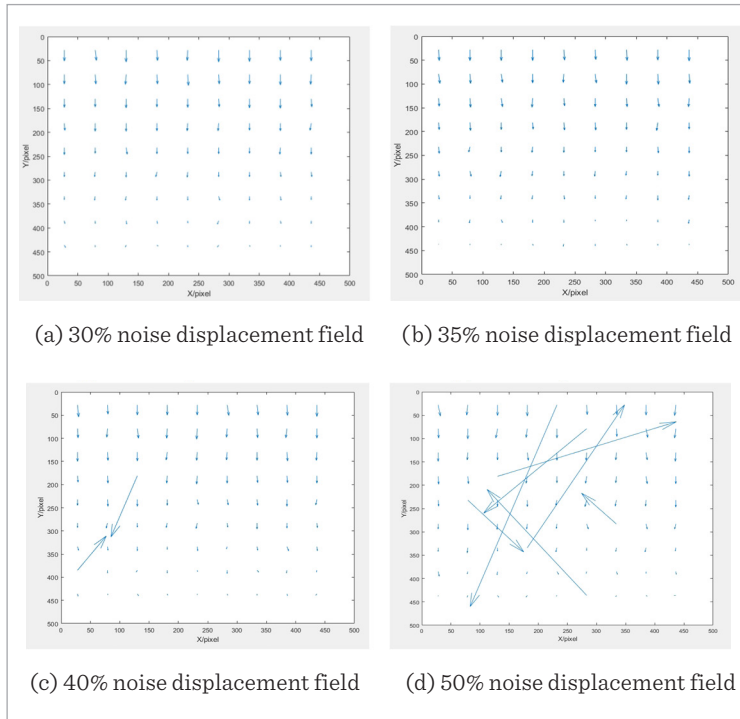
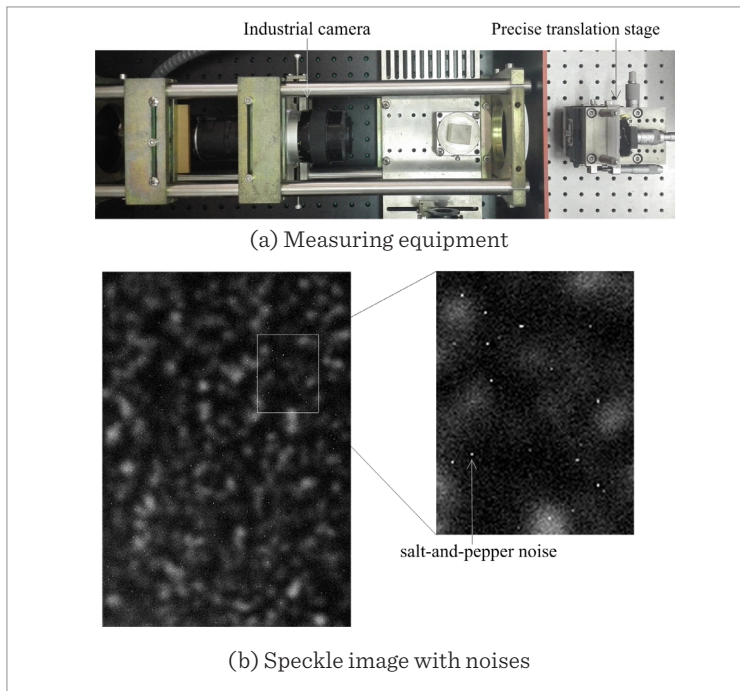


Figure 9

Displacement field of different noises

**Figure 10**

Measuring equipment and a speckle image with noises



The conclusions from these comparisons are as follows: (1) the DISRC can deal with well 21% noise level; (2) The displacement filed by DISRC is very stable.

5. Displacement Measurement Case

5.1. Platform

To verify the validity of DISRC using actual speckle images with salt-and-pepper noise, a displacement measurement case was designed. We utilized optical measuring equipment consisting of an industrial camera and a precise translation stage as shown in Figure 10 (a), and then a host computer saved the 8-bits gray digital speckle images obtained.

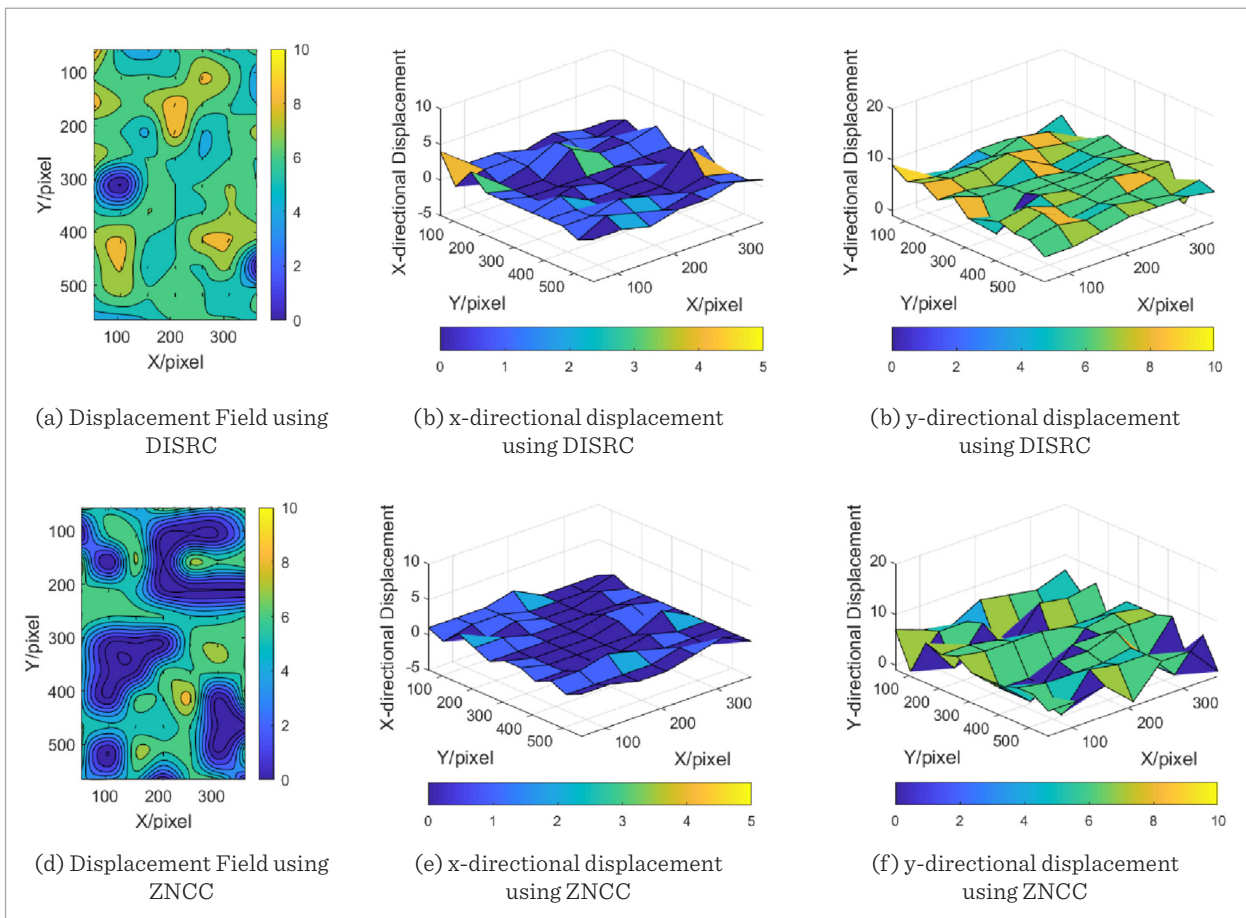
A speckle surface object was photographed before and after slightly moving the object using the precise translation stage. The exposure time was set 1.28s to allow for the occurrence of salt-and-pepper noise as shown in Figure 10 (b), the right picture of which is a detail of the speckle image with some salt and pepper noises. The subset size is 51×51 in all of the experiments. Results using DISRC and ZNCC would be compared and analyzed.

5.2. Result and Analysis

The DISRC and ZNCC were used to compute the displacement field when both the reference and target speckle images were contaminated by salt-and-peppernoise, and the result is shown in Figure 11 (a)-(c) are the results obtained using DISRC, while Figure 11 (d)-(f) are the results obtained using ZNCC. Figure 11 (a) and (d) are the final effect of displacement field, including the displacement vector and 10-rank contour line of y vectors' size. Figure 11 (b) and (e) are the -directional displacement, (c) and (f) are the -directional displacement.

Figure 11

Comparisons between DISRC and ZNCC with 51×51subset size



As the final results using DISRC and ZNCC in Figure 11 (a) and (d), most of the vector sizes using DISRC is about 6 pixels, while a part of the vector size using ZNCC is 0 pixel. The mean vector size obtained using DISRC is 6.15, with a variance of 2.25, while a mean of 4.17 and variance of 8.03 were obtained using ZNCC. Therefore, we see that the effect of the displacement field using DISRC is better than ZNCC, when both the reference and the target speckle images are contaminated by salt-and-pepper noise.

6. Conclusion

Salt-and-pepper noise, an unavoidable type of noise in digital images, is troublesome to process in digital image correlation techniques. Traditional DIC using

ZNCC is sensitive to this kind of noise, which leads to incorrect displacement field. While the DISRC can successfully deal with the noise, but it need more time to compute the rank.

We focus our attention on the robustness of DISRC and accelerating computations. The robustness of DISRC was studied in theory and a preliminary verification was performed. The DISRC is an effective and strong anti-interference digital image correlation technique, and it is very important for practical engineering applications, especially in complex environments. Parallelization is used to accelerate the DISRC calculations in our fast frame, including precomputing ranks and computing displacement field, and the speed-up effect is suitable for DISRC application. In the future, more applications will be investigated.

Acknowledgement

This work was supported in part by the National Natural Science Foundation of China under Grant no. 62073090, U22A2062, in part by the Natural Science Foundation of Guangdong Province of China under Grant no. 2019A1515010700, in part by the Key (nat-

ural) Project of Guangdong Provincial under Grant no. 2019KZDXM020, 2019KZDZX1004, 2019KZDZX1042, in part by the Introduction of Talents Project of Guangdong Polytechnic Normal University of China under Grant no. 991512203, 991560236, in part by Special projects in key areas of ordinary colleges and universities in Guangdong Province no. 2020ZDZX2014.

References

1. Bay, B. K. Methods and Applications of Digital Volume Correlation. *The Journal of Strain Analysis for Engineering Design*, 2008, 43(8), 745-760. <https://doi.org/10.1243/03093247JSA436>
2. Bian, X., Saleh, A. A., Pereloma, E. V., Davier, C. H. J., Gazder, A. A. A Digital Image Correlation Study of a NiTi Alloy Subjected to Monotonic Uniaxial and Cyclic Loading-Unloading in Tension. *Materials Science and Engineering: A*, 2018, 726, 102-112. <https://doi.org/10.1016/j.msea.2018.04.081>
3. Bomarito, G. F., Hochhalter, J. D., Ruggles, T. J., Cannon, A. H. Increasing Accuracy and Precision of Digital Image Correlation Through Pattern Optimization. *Optics and Lasers in Engineering*, 2017, 91, 73-85. <https://doi.org/10.1016/j.optlaseng.2016.11.005>
4. Bossuyt, S. Optimized Patterns for Digital Image Correlation. *Imaging Methods for Novel Materials and Challenging Applications*, 2013, 3, 239-248. https://doi.org/10.1007/978-1-4614-4235-6_34
5. Chen, D., Sun, S., Dulieu-Barton, J. M., Li, Q., Wang, W. Crack Growth Analysis in Welded and Non-welded T-joints Based on Lock-in Digital Image Correlation and Thermoelastic Stress Analysis. *International Journal of Fatigue*, 2018, 110, 172-185. <https://doi.org/10.1016/j.ijfatigue.2018.01.020>
6. Cai, L., Yang, J., Dong, S., Jiang, Z. GPU Accelerated Parallel Reliability-Guided Digital Volume Correlation with Automatic Seed Selection Based on 3D SIFT. *Parallel Computing*, 2021, 108, 102824. <https://doi.org/10.1016/j.parco.2021.102824>
7. Chapelier, M., Bouclier, R., Passieux, J. C. Free-Form Deformation Digital Image Correlation (FFD-DIC): A Non-invasive Spline Regularization for Arbitrary Finite Element Measurements. *Computer Methods in Applied Mechanics and Engineering*, 2021, 384, 113992. <https://doi.org/10.1016/j.cma.2021.113992>
8. Chen, X., Tian, G., Wu, J., Tang, C., Li, K. Feature-based Registration for 3D Eddy Current Pulsed Thermogra-
phy. *IEEE Sensors Journal*, 2019, 19(16), 6998-7004. <https://doi.org/10.1109/JSEN.2019.2911699>
9. Chen, D. J., Chiang, F. P., Tan, Y. S., Don, S. Digital Speckle-Displacement Measurement Using a Complex Spectrum Method. *Applied Optics*, 1993, 32(11), 1839-1849. <https://doi.org/10.1364/AO.32.001839>
10. Davis, C. Q., Freeman, D. M. Statistics of Subpixel Registration Algorithms Based on Spatiotemporal Gradients or Block Matching. *Optical Engineering*, 1998, 37(4), 1290-1298. <https://doi.org/10.1117/1.601966>
11. Dong, Y. L., Pan, B. A Review of Speckle Pattern Fabrication and Assessment for Digital Image Correlation. *Experimental Mechanics*, 2017, 57(8), 1161-1181. <https://doi.org/10.1007/s11340-017-0283-1>
12. Finlayson, G., Hordley, S., Schaefer, G., Tian, G. Y. Illuminant and Device Invariant Colour Using Histogram Equalisation. *Pattern Recognition*, 2005, 38(2), 179-190. <https://doi.org/10.1016/j.patcog.2004.04.010>
13. Gustafson, J. L. Reevaluating Amdahl's Law. *Communications of the ACM*, 1988, 31(5), 532-533. <https://doi.org/10.1145/42411.42415>
14. He, W., Wang, C., Wang, S., Yao, L., Wang, L., Xie, D. Characterizing and Predicting the Tensile Mechanical Behavior and Failure Mechanisms of Notched FMLs-Combined with DIC and Numerical Techniques. *Composite Structures*, 2020, 254, 112893. <https://doi.org/10.1016/j.compstruct.2020.112893>
15. Hild, F., Misra, A. Multiscale DIC Applied to Pantographic Structures. *Experimental Mechanics*, 2021, 61(2), 431-443. <https://doi.org/10.1007/s11340-020-00636-y>
16. Huang, W., Wang, Q., Xu, W., Hu, Z., Zhou, Y. Robust Digital Imaging Spearman's Rho Correlation for Pepper and Salt Noise. *Optics and Precision Engineering*, 2015, 23(6), 1800-1806. <https://doi.org/10.3788/OPE.20152306.1800>
17. Hu, X., Xie, Z., Liu, F. Assessment of Speckle Pattern Quality in Digital Image Correlation from the Perspective

- of Mean Bias Error. *Measurement*, 2021, 173, 108618. <https://doi.org/10.1016/j.measurement.2020.108618>
18. Huang, P., Guo, Z. Li-ion Distribution and Diffusion-Induced Stress Calculations of Particles Using an Image-Based Finite Element Method. *Mechanics of Materials*, 2021, 157, 103843. <https://doi.org/10.1016/j.mechmat.2021.103843>
 19. Henriques, J., Xavier, J., Andrade-Campos, A. Identification of Orthotropic Elastic Properties of Wood by a Synthetic Image Approach Based on Digital Image Correlation. *Materials*, 2022, 15(2), 625. <https://doi.org/10.3390/ma15020625>
 20. Hua, T., Xie, H., Wang, S., Hu, Z., Chen, P., Zhang, Q. Evaluation of the Quality of a Speckle Pattern in the Digital Image Correlation Method by Mean Subset Fluctuation. *Optics & Laser Technology*, 2011, 43(1), 9-13. <https://doi.org/10.1016/j.optlastec.2010.04.010>
 21. Huang, J., Pan, X., Peng, X., Zhu, T., Qin, L., Xiong, C., Fang, J. High-Efficiency Cell-Substrate Displacement Acquisition Via Digital Image Correlation Method Using Basis Functions. *Optics and lasers in engineering*, 2010, 48(11), 1058-1066. <https://doi.org/10.1016/j.optlaseng.2009.12.009>
 22. Huang, J. W., Zhang, L. Q., Jiang, Z. Y., Dong, S. B., Chen, W., Liu, Y. P., Liu, Z. J., Zhou, L. C., Tang, L. Q. Heterogeneous Parallel Computing Accelerated Iterative Subpixel Digital Image Correlation. *Science China Technological Sciences*, 2018, 61(1), 74-85. <https://doi.org/10.1007/s11431-017-9168-0>
 23. Huang, W., Wang, Q., Xu, W., Zhou, Y. Robustness Analysis of Digital Image Spearman's Rho Correlation. *A A*, 2016, 2(2), 2. <https://doi.org/10.2991/aest-16.2016.29>
 24. Jiang, Z., Kemao, Q., Miao, H., Yang, J., Tang, L. Path-Independent Digital Image Correlation with High Accuracy, Speed and Robustness. *Optics and Lasers in Engineering*, 2015, 65, 93-102. <https://doi.org/10.1016/j.optlaseng.2014.06.011>
 25. Kefal, A., Diyaroglu, C., Yildiz, M., Oterkus, E. Coupling of Peridynamics and Inverse Finite Element Method for Shape Sensing and Crack Propagation Monitoring of Plate Structures. *Computer Methods in Applied Mechanics and Engineering*, 2022, 391, 114520. <https://doi.org/10.1016/j.cma.2021.114520>
 26. Lecompte, D., Smits, A., Bossuyt, S., Sol, H., Vantomme, J., Hemelrijck, D. V., Habraken, A. M. Quality Assessment of Speckle Patterns for Digital Image Correlation. *Optics and Lasers in Engineering*, 2006, 44(11), 1132-1145. <https://doi.org/10.1016/j.optlaseng.2005.10.004>
 27. Peters, W. H., Ranson, W. F. Digital Imaging Techniques in Experimental Stress Analysis. *Optical Engineering*, 1982, 21(3), 427-431. <https://doi.org/10.1117/12.7972925>
 28. Pan, B., Qian, K., Xie, H., Asundi, A. Two-Dimensional Digital Image Correlation for In-plane Displacement and Strain Measurement: A Review. *Measurement Science and Technology*, 2009, 20(6), 062001. <https://doi.org/10.1088/0957-0233/20/6/062001>
 29. Pan, B., Wu, D., Yu, L. Optimization of a Three-Dimensional Digital Image Correlation System for Deformation Measurements in Extreme Environments. *Applied Optics*, 2012, 51(19), 4409-4419. <https://doi.org/10.1364/AO.51.004409>
 30. Pan, B. Digital Image Correlation for Surface Deformation Measurement: Historical Developments, Recent Advances and Future Goals. *Measurement Science and Technology*, 2018, 29(8), 082001. <https://doi.org/10.1088/1361-6501/aac55b>
 31. Pan, B., Xie, H., Guo, Z., Hua, T. Full-field Strain Measurement Using a Two-Dimensional Savitzky-Golay Digital Differentiator in Digital Image Correlation. *Optical Engineering*, 2007, 46(3), 033601. <https://doi.org/10.1117/1.2714926>
 32. Pan, B. Bias Error Reduction of Digital Image Correlation Using Gaussian Pre-filtering. *Optics and Lasers in Engineering*, 2013, 51(10), 1161-1167. <https://doi.org/10.1016/j.optlaseng.2013.04.009>
 33. Pan, B., Xie, H., Wang, Z., Qian, K., Wang, Z. Study on Subset Size Selection in Digital Image Correlation for Speckle Patterns. *Optics Express*, 2008, 16(10), 7037-7048. <https://doi.org/10.1364/OE.16.007037>
 34. Pan, B., Lu, Z., Xie, H. Mean Intensity Gradient: An Effective Global Parameter for Quality Assessment of The Speckle Patterns Used in Digital Image Correlation. *Optics and Lasers in Engineering*, 2010, 48(4), 469-477. <https://doi.org/10.1016/j.optlaseng.2009.08.010>
 35. Pan, B. Reliability-guided Digital Image Correlation for Image Deformation Measurement. *Applied Optics*, 2009, 48(8), 1535-1542. <https://doi.org/10.1364/AO.48.001535>
 36. Pan, B., Tian, L. Superfast Robust Digital Image Correlation Analysis with Parallel Computing. *Optical Engineering*, 2015, 54(3), 034106. <https://doi.org/10.1117/1.OE.54.3.034106>
 37. Pan, B. Recent Progress in Digital Image Correlation. *Experimental Mechanics*, 2011, 51(7), 1223-1235. <https://doi.org/10.1007/s11340-010-9418-3>
 38. Pan, B., Xie, H., Wang, Z. Equivalence of Digital Image Correlation Criteria for Pattern Matching. *Applied Optics*, 2010, 49(28), 5501-5509. <https://doi.org/10.1364/AO.49.005501>
 39. Sutton, M. A., Wolters, W. J., Peters, W. H., Ranson, W. F., Mcneill, S. R. Determination of Displacements Using an Improved Digital Correlation Method. *Image*

- and Vision Computing, 1983, 1(3), 133-139. [https://doi.org/10.1016/0262-8856\(83\)90064-1](https://doi.org/10.1016/0262-8856(83)90064-1)
40. Su, Z., Pan, J., Zhang, S., Wu, S., Yu, Q., Zhang, D. Characterizing Dynamic Deformation of Marine Propeller Blades with Stroboscopic Stereo Digital Image Correlation. *Mechanical Systems and Signal Processing*, 2022, 162, 108072. <https://doi.org/10.1016/j.ymssp.2021.108072>
 41. Sun, Y., Pang, J. H. L., Wong, C. K., Su, F. Finite Element Formulation for a Digital Image Correlation Method. *Applied Optics*, 2005, 44(34), 7357-7363. <https://doi.org/10.1364/AO.44.007357>
 42. Segalman, D. J., Woyak, D. B., Rowlands, R. E. Smooth Spline-like Finite-element Differentiation of Full-field Experimental Data Over Arbitrary Geometry. *Experimental Mechanics*, 1979, 19(12), 429-437. <https://doi.org/10.1007/BF02326046>
 43. Sutton, M. A., Turner, J. L., Bruck, H. A., Chae, T. A. Full-field Representation of Discretely Sampled Surface Deformation for Displacement and Strain Analysis. *Experimental Mechanics*, 1991, 31(2), 168-177. <https://doi.org/10.1007/BF02327571>
 44. Song, J., Yang, J., Liu, F., Lu, K. Quality Assessment of Laser Speckle Patterns for Digital Image Correlation by a Multi-Factor Fusion Index. *Optics and Lasers in Engineering*, 2020, 124, 105822. <https://doi.org/10.1016/j.optlaseng.2019.105822>
 45. Stoilov, G., Kavardzhikov, V., Pashkouleva, D. A Comparative Study of Random Patterns for Digital Image Correlation. *Journal of Theoretical and Applied Mechanics*, 2012, 42(2), 55. <https://doi.org/10.2478/v10254-012-0008-x>
 46. Shao, X., Dai, X., He, X. Noise Robustness and Parallel Computation of the Inverse Compositional Gauss-Newton Algorithm in Digital Image Correlation. *Optics and Lasers in Engineering*, 2015, 71, 9-19. <https://doi.org/10.1016/j.optlaseng.2015.03.005>
 47. Shevlyakov, G. L., Vilchevski, N. O. Robustness in Data Analysis: Criteria and Methods. Netherlands: Walter de Gruyter, 2002. <https://doi.org/10.1515/9783110936001>
 48. Schmogrow, R., Nebendahl, B., Winter, M., Josten, A., Hillerkuss, D., Koenig, S., Meyer, J., Dreschmann, M., Huebner, M., Koos, C., Becker, J., Freude, W., Leuthold, J. Error Vector Magnitude as a Performance Measure for Advanced Modulation Formats. *IEEE Photonics Technology Letters*, 2011, 24(1), 61-63. <https://doi.org/10.1109/LPT.2011.2172405>
 49. Vormwald, M., Hos, Y., Freire, J. L. F., Giancarlo, L. G. G., Jorge, G. D. Crack Tip Displacement Fields Measured by Digital Image Correlation for Evaluating Variable Mode-Mixity During Fatigue Crack Growth. *International Journal of Fatigue*, 2018, 115, 53-66. <https://doi.org/10.1016/j.ijfatigue.2018.04.030>
 50. Xu, W. A Review on Correlation Coefficients. *Journal of Guangdong University of Technology*, 2012, 29(3), 12-17.
 51. Xu, W., Hou, Y., Hung, Y. S., Zou, Y. X. A Comparative Analysis of Spearman's Rho and Kendall's Tau in Normal and Contaminated Normal Models. *Signal Processing*, 2013, 93(1), 261-276. <https://doi.org/10.1016/j.sigpro.2012.08.005>
 52. Yamaguchi, I. A Laser-speckle Strain Gauge. *Journal of Physics E: Scientific Instruments*, 1981, 14(11), 1270. <https://doi.org/10.1088/0022-3735/14/11/012>
 53. Yang, R. A Regularized Finite-Element Digital Image Correlation for Irregular Displacement Field. *Optics and Lasers in Engineering*, 2014, 56, 67-73. <https://doi.org/10.1016/j.optlaseng.2013.12.013>
 54. Yaofeng, S., Pang, J. H. L. Study of Optimal Subset Size in Digital Image Correlation of Speckle Pattern Images. *Optics and Lasers in Engineering*, 2007, 45(9), 967-974. <https://doi.org/10.1016/j.optlaseng.2007.01.012>
 55. Yang, X., Chen, X., Xi, J. Error Suppression for Speckle Correlation-Based 3D Shape Measurement Via Dynamic Shape Function Selection. *Optics Communications*, 2022, 508, 127584. <https://doi.org/10.1016/j.optcom.2021.127584>
 56. Zhao, J., Zeng, P., Pan, B., Lei, L., Du, H., He, W., Liu, Y., Xu, Y. Improved Hermite Finite Element Smoothing Method for Full-Field Strain Measurement Over Arbitrary Region of Interest in Digital Image Correlation. *Optics and Lasers in Engineering*, 2012, 50(11), 1662-1671. <https://doi.org/10.1016/j.optlaseng.2012.04.008>
 57. Zhong, F., Quan, C. Efficient Digital Image Correlation Using Gradient Orientation. *Optics and Laser Technology*, 2018, 106, 417-426. <https://doi.org/10.1016/j.optlastec.2018.04.024>
 58. Zhang, L., Wang, T., Jiang, Z., Kemao, Q., Liu, Y., Liu, Z., Tang, L., Dong, S. High Accuracy Digital Image Correlation Powered by GPU-Based Parallel Computing. *Optics and Lasers in Engineering*, 2015, 69, 7-12. <https://doi.org/10.1016/j.optlaseng.2015.01.012>
 59. Zhou, Y., Chen, Y. Q. Propagation Function for Accurate Initialization and Efficiency Enhancement of Digital Image Correlation. *Optics and Lasers in Engineering*, 2012, 50(12), 1789-1797. <https://doi.org/10.1016/j.optlaseng.2012.06.017>

